Chapter 3

Experimental Reactor Design and AAS Measurement Implementation

In this chapter, we will present our work on the development of an observable untra-high vacuum chemical vapor deposition (UHVCVD) reactor. This design features integration of atomic absorbance spectroscopy (AAS) measurement for improving reproducibility and observably. We will furthermore validate the fluxes model presented in Chapter 2 and the AAS measurements using an experimental setup. The chapter is structured as follows. In Section 3.1, we will explain the AAS measurement principle in detail and motive our choice for the AAS sensor further. Section 3.2 will be used to explain the design of our experiment, the experimental setup and to discuss assumptions and simplifications. Subsequently, we use Section 3.3 to explain our realizations of the fluxes model, a benchmark moles model and the mathematics involved in obtaining a pressure measurement out of the measured AAS signal. Following this, our experimental results are presented in Section 3.4. We round up with some concluding remarks in Section 3.5.

3.1 Atomic absorption spectroscopy preliminaries

We will use this section to motivate our choice for the AAS technology by comparing it with other candidate technologies. We will furthermore provide an in-depth explanation of the principles and phenomena used in AAS and some of the important design considerations.

3.1.1 Motivation of AAS sensor selection

Let us motivate our choice for the AAS implementation by considering it in the broader perspective of realizing an observable[1] UHVCVD reactor. To this end, we will start by considering all relevant states that we are interested in observing, in order to narrow down to partial pressures. We then subsequently compare measurement techniques for the partial pressures in order to present our motivated choice for the AAS technique.

[1] Here, observable refers to the ability of reconstructing all state variables based on the given measured variables.

The measurable state variables that are relevant for realizing an observable UHV-CVD process are: (i) temperatures, (ii) film characteristics (such as, thickness, layer composition, etc.) and (iii) precursor partial pressures (or fluxes) at the substrate. The first and third variables together affect the chemical reactions that are the depositions, which in turn affects the second one. This is in accordance with the modeling for UHVCVD as in (Greve and Racanelli 1991). Measuring temperatures can be done through contact (thermocouple) and optically (pyrometer). Both of these methods are well established and compatible with ultra-high vacuum (UHV). Temperature control is typically performed by placing PID-controlled heating or cooling elements at locations of interest, such as the substrate. Such a form of control is rudimentary but works well, in particular in combination with a reference manager. Measuring layer characteristics (the second measured state variable) can be done optically through the use of ellipsometry, reflection or transmission measurements (as for example implemented in (Middlebrooks and Rawlings 2007)). The techniques are well established but require application dependent models to relate measured variables to film characteristics. Also, any control action based on a real-time layer characteristic measurement will demand a change in pressure or temperature (through the reference manager, for example), since these are the variables that affect the chemical reactions during the depositions. We therefore consider such a controller to be of a higher hierarchical level than the partial pressure or temperature controllers in such a process. This causes its effectiveness to be dependent on the performance of the lower level pressure and temperature controllers. In contrast to the above, a method for measuring the precursor partial pressures (the third measured state variable) is not clearly visible in the literature. The exposition above motivates our interest in the implementation of a real-time precursor partial pressure measurement for a UHV-CVD reactor. Such a measurement can accordingly improve the reproducibility and observability for such a process.

The main techniques for real-time partial pressure or flux measurements that are suitable for vacuum conditions are mass spectrometry (MS) (Chang et al. 1973), electron impact emission spectrometry (EIES) (Lu et al. 1977) and atomic absorption spectrometry (AAS) (Klausmeier-Brown et al. 1992, Lu and Guan 1995, Kasai and Sakai 1997, Vignaud and Mollot 2007, Du et al. 2014). Both MS and EIES are material specific and highly sensitive. However, they require physical presence of a sensor with a heated filament in the deposition chamber and the measurement is therefore intrusive and places restrictions on the thermal budget. Moreover, the sensor will need to be heated with the rest of the reactor, which will therefore restrict the thermal budget further. AAS is a very sensitive and selective atom detection technique that can operate at any pressure. It is furthermore non-intrusive and therefore places little constraints on the system design and thermal budget. This, combined with the (typical) atomic reactant presence in the deposition chamber makes the AAS measurement a suitable measuring technique for UHVCVD.

3.1.2 AAS measurement technique

AAS is an optical technique that is applied in the closely related MBE process (some examples can be found in (Klausmeier-Brown et al. 1992, Lu and Guan 1995, Kasai and Sakai 1997, Vignaud and Mollot 2007, Du et al. 2014)). The AAS technique relies on insights from quantum mechanics. These mechanics describe that each atom can have different quantum states, expressed in electron orbitals. These quantum states in turn have fixed energy levels which have specific energy differences from each other. Accordingly, changing between these orbital states requires these energy differences to be met, which occurs by absorbing or emitting a photon. For the absorption, if the photon energy does not match this energy difference between the two quantum states, then the change in quantum state is not possible and the photon will not be absorbed. For the emission, only a photon of the specified energy can be emitted by the change in quantum state. The photon energy E is furthermore uniquely related to its wavelength l_w, through the Planck-Einstein relation

$$E = \frac{h_p c}{l_w}, \tag{3.1}$$

with h_p the Planck's constant and c the speed of light through a vacuum. We accordingly have that specific elements (atoms) can absorb specific wavelengths in a very selective manner. The required amount of energy or wavelength for atomic detection are known for most elements. In AAS, this principle is exploited by measuring absorbance of the specific, corresponding wavelength(s) of light that has passed through an atom cloud containing specific element(s).

The quality of the AAS measurement largely depends on the bandwidth or selectivity of wavelengths that are present in the light bundle used for the measurements. If this bandwidth is too broad, a poor signal to noise ratio may result. This occurs because there is a relatively high total light intensity of which only a small fraction becomes absorbed by the atom cloud. This therefore causes the natural noise to be relatively high while the changes that are to be observed become relatively small. On the other hand, if the bandwidth is narrow, we have relatively large changes in signal due to the atomic absorptions, while the natural noise in the light still remains a small fraction of the total light intensity. Such a narrow bandwidth is typically referred to as a narrow line, which refers in turn to peaks such as shown in Fig. 3.1. Obtaining such a narrow line or bandwidth is done by having a selective light source, that produces an isolated light intensity peak at the wavelength of interest, in combination with a very narrow filter or monochromator to further select the desired wavelength at a later stage.

For the light source, a hollow-cathode lamp (HCL) is typically used. Such a lamp is a glass tube containing an anode, a hollow-cathode and a (noble) buffer gas. A large voltage across the anode and cathode will cause the buffer gas to ionize, hence creating a plasma. The ions are subsequently accelerated to the hollow-cathode, which causes atoms to be sputtered off. The buffer gas and the sputtered atoms

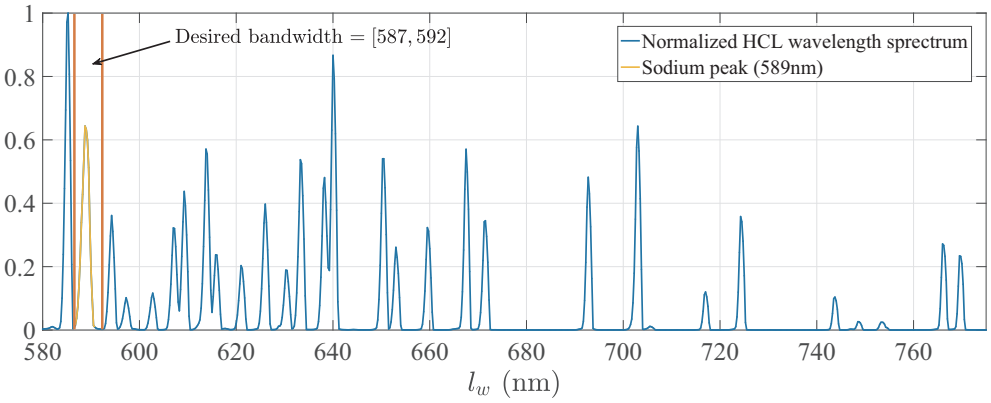

Figure 3.1: Wavelength spectrum for sodium HCL

We show the wavelength spectrum of a sodium hollow-cathode lamp (HCL). The spectrum shows multiple peaks for different elements present in the plasma of the hollow-cathode lamp. The height of the peak indicates the relative light intensity, which has been normalized for the highest peak in the spectrum. For measuring sodium, we would be interested in isolating the sodium peak (at $l_w = 589nm$) with a bandpass filter or monochromator, so that we obtain a satisfactory the signal-to-noise ratio.

are in turn excited by collisions in the plasma. This excitation is the process of these atoms being promoted to higher orbitals in accordance with the quantum mechanical principles explained earlier. This excitation is however of a temporary nature and when the atoms decay to a lower orbital they release a photon with energy equal to this difference. Such a lamp will accordingly send out wavelengths determined by the atomic and molecular presence in the lamp materials. By choosing a proper collection of these components, including the element that is to be detected, one can obtain a wavelength spectrum that has an isolated peak at the wavelength of interest. An example of such a wavelength spectrum for a sodium hollow-cathode lamp is shown in Fig. 3.1. For this exemplary wavelength spectrum, we have a sodium peak falling in the bandwidth $l_w = [587, 592]$ nm. We are hence interested in cutting off all wavelengths outside this bandwidth. A combination of filters or a monochromator can accordingly be used to achieve this.

The AAS technique has seen several improvements from its basic form. One of these improvements is the implementation of a dual beam set-up (Du et al. 2014). This setup utilizes a beam-splitter to detect and correct for changes in the light source. For a hollow-cathode lamp such changes can either be caused by degradation of the lamp, which causes the intensity of the light to change, or by plasma drift, which causes the optical alignment to change. The former can be corrected for with the dual-beam setup, the latter remains a factor influencing the measurements. Another improvement is implementation of real-time noise filtering (Kasai and Sakai 1997). This can be done through lock-in amplification when the signal-

to-noise ratio is poor and when the noise has a high frequency. A shutter typically suffices for good signal-to-noise ratios with significant changes in background light (e.g. light reaching the photo-diode that is not generated by the AAS light source).

3.2 Experimental design and scope

In this section we will describe our experimental scope and setup, the AAS sensor design and calibration principle, and the simplifications and assumptions that we make.

3.2.1 Experimental scope

Our experiment has the purpose of validating the AAS measurements applicability and part of the flux dynamical model for characterization of partial pressures such as are present in UHVCVD. We restrict the scope of the experiment to the vapor pressure regime. This has the advantage that (with reference to Section 2.2): (i) we can use existing vapor pressure functions for derivation of the sorption functions, (ii) we can perform the assessment of the AAS sensor and the models simultaneously and (iii) we can proceed without identifying the input function, since we do not need to characterize the evaporation phenomena. In the vapor pressure regime, we are accordingly interested in showing consistency of the AAS measurement and to show that our fluxes model can estimate the considered partial pressure. We will use sodium for this experiment, since it has a relatively high vapor pressure and because such evaporation sources are commercially available.

3.2.2 Experimental setup design

The experimental setup is shown in Fig. 3.2. The setup consists of three layers. The first and outermost layer is the thermal layer, which is used for heating actuation. This layer facilitates the hot wall processing and high temperature cleaning of the reactor, which is required for obtaining UHV conditions. The second layer is the vacuum layer. The vacuum layer is formed by a stainless steel vacuum chamber, which is attached to the vacuum pumps. The vacuum layer is outfitted with various viewports and feedthroughs for signal interaction. The third and innermost layer is the chemical layer. The chemical layer allows for building up of sodium pressure by providing an environment with a desired leakage (e.g. such that the sodium cannot be pumped away easily). Such a layer is often referred to as the deposition chamber and is located inside the vacuum. The set $\mathbb{M}$ (as introduced in Section 2.1) is the inside surface of this chamber for this experiment. We use a glass cylinder as deposition chamber, which facilitates mounting of the sodium evaporation sources. The glass is required because the transparency allows us to perform the optical AAS measurements.

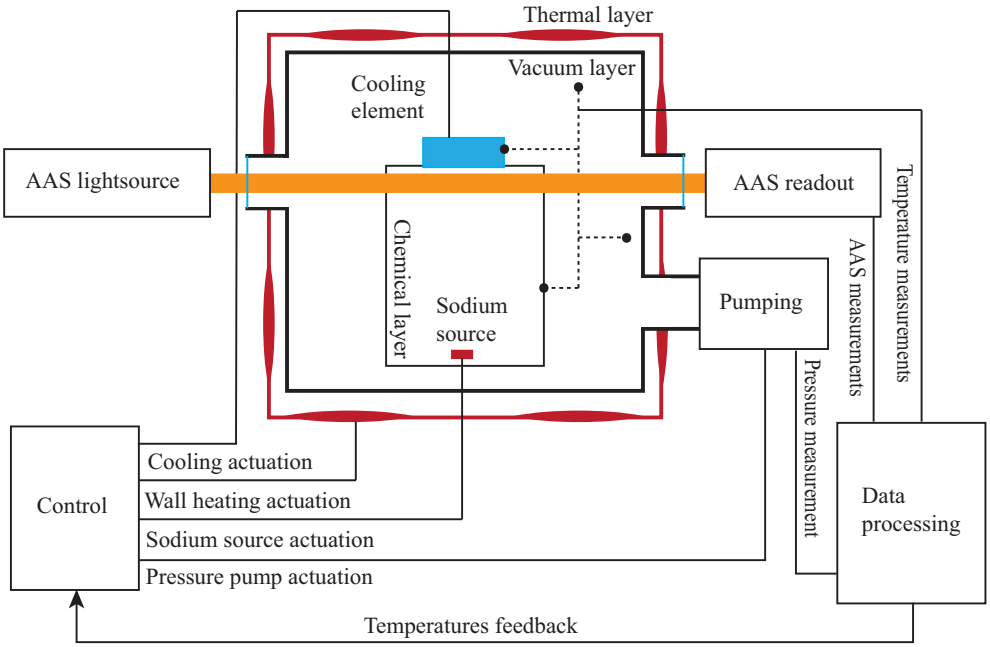

Figure 3.2: Schematic of experimental UHVCVD setup with AAS

A schematic of the experimental setup used in this thesis chapter is shown. The setup consists of three fundamental layers, which act as boundaries for the temperature (thermal layer), the pressure (vacuum layer) and for the sodium atoms (chemical layer). The design allows for real-time measurements of temperature, reactor pressure and sodium pressure (through AAS). The AAS components are discussed in more detail in Section 3.2.2 and Fig. 3.3. The setup actuators are the pressure pumps, the sodium source, the wall heating elements and the cooling element. The cooling element is placed so that it directly influences vapor pressures inside the chemistry layer.

The design facilitates the following real-time measurements: (i) reactor temperatures, (ii) cooling element temperature, (iii) sodium pressure and (iv) pump pressure. The temperatures are measured with K-type thermocouples, the sodium pressure is measured through AAS and the pump pressure is measured with a hot-filament ionization gauge. Read-out is done with modules supplied by National Instruments (NI USB-6211) for the pressures and Measurement Computing (MC USB-TC) for the temperatures. All measured signals are handled and manipulated in Labview.

The following actuators are used: (i) heating elements forming the thermal layer, (ii) sodium evaporation sources, (iii) a proportional pressure valve connected to the cooling element and (iv) pressure pumps. The heating elements are part of a separate PID control loop so that we can directly control the temperature of the thermal layer. These heating elements allow for heating above 330 deg C everywhere inside the thermal layer. The sodium source is current controlled and the current is set directly. The cooling element air flow is controlled with a proportional valve (Festo VEAB).

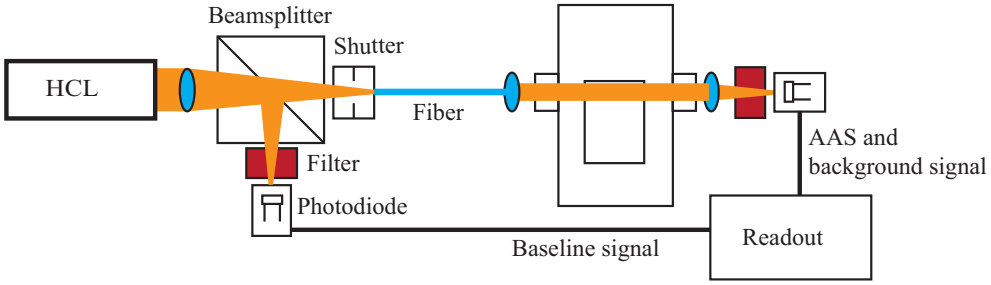

Figure 3.3: Detailed view of AAS components in experimental setup

A schematic representation of the AAS sensor design is shown. The AAS light source is a hollow-cathode lamp (HCL). The light generated by this lamp is focused and sent through a beamsplitter. From there, one of the bundles is filtered and converted to an electronic signal. This signal is the baseline signal. The other bundle is sent through a shutter and into an optical fiber. This light is subsequently focused through the deposition chamber, which contains the atom cloud. After this, the light is filtered and converted to an electronic signal. This signal is the AAS signal when the shutter is open and the background signal when the shutter is closed. The AAS sensor is integrated in the setup shown in Fig. 3.2.

This flow is regulated with a proportional controller so that we can set the cold spot temperature as an input. We use a diaphragm pump and a turbo molecular pump (both Pfeiffer) to attain the UHV conditions. The pumps allow for pressures $< 10^{-7}$ Pa after bake-out. The actuation signals are generated in Labview and applied with the previously mentioned NI USB-6211 module and the MC USB-3103 module from Measurement Computing.

The full AAS sensor design is shown in Fig. 3.3. The design features a dual beam setup (as in (Du et al. 2014)), to correct for changes in light intensity generated by the lamp. We furthermore incorporate an electronic shutter, to correct each sample for changes in background light intensity. As light source we use a sodium hollow-cathode lamp supplied by Hamamatsu, where we further select the sodium peak (around 589nm, see Fig. 3.1) with optical band-pass filters. The measured signal from the photo-diodes is pre-amplified before readout.

3.2.3 Other design choices, simplifications and assumptions

In order to maintain the vapor pressure regime inside the deposition chamber, we design the deposition chamber with minimal leakage. And, as mentioned in Section 3.2.1, we can restrict ourselves to the situation where no new evaporations occur for this experiment. This implies that, with reference to (2.5), we have that $L \approx 0$ and $g(u(t), t) = 0$. We accordingly obtain simplified dynamics which allow us to focus on the role of A and $f(\cdot)$. The model can, at a later stage, be extended to include L and $g(u(t), t)$, using the insights we obtain on A and $f(\cdot)$ in this paper.

We have accordingly allowed ourselves to eliminate the original input $u(t)$. How-

ever, our experimental setup features direct control over the cold spot temperature T_c. We can thus consider a new input $\dot{T}_r = \nu(t)$, where T_r is a temperature reference signal supplied to the cold spot. For T_a, we expect that the average temperature in the atom cloud will satisfy a weighted average temperature of the surfaces facing the atom cloud. The weight is dependent on residence time on each surface, and cold surfaces will therefore have a stronger influence on the temperature than hot surfaces. For ease of reasoning, we will assume that $T_a = T_c$, with T_c the cold spot temperature. We will furthermore assume that the temperatures of the surfaces facing the atom cloud, other than the temperature of the cold spot, are constant.

In the vapor pressure regime, a bulk material of precursor atoms are present on the coldest surface of the reactor. Such a bulk material will by approximation have a constant number of atoms that are exposed to the vacuum, depending on surface area, roughness and porosity. Furthermore, only atoms exposed to the vacuum can desorb from this bulk material. This phenomena causes a decoupling of the dynamics of x and s through $f(\cdot)$, since s will be represented in $f(\cdot)$ through a saturation function which is consequently saturated in the vapor pressure regime. Moreover, the vapor pressure function that we will use in the sequel does not directly provide required information on the sorption that occurs. We will accordingly not incorporate s as a state variable for this experiment.

3.3 Modeling for experimentation

We will discuss the modeling related to the AAS signal interpretation and the implementation of the models from Chapter 2 here. To asses the sensor and model performances, we will compare: (i) the fluxes model (as in (2.5)), (ii) the moles model having N as state (as in (2.3)), (iii) the measured sodium pressure by AAS and (iv) the theoretical vapor pressure (based on cold spot temperature). This chapter is accordingly used to explain how we obtain these signals. The simplifications and assumptions that we have discussed in the previous section have direct implications on the modeling for our experiment.

3.3.1 AAS signal interpretation

For the sensor model of our AAS setup we can use a modification of the formulas provided in (Du et al. 2014). Accordingly, we have for very low fluxes and under monochromatic radiation the Beer-Lambert law for absorbance given by

$$\lambda(t) = \log_{10}\left(\frac{Q_{in}(t)}{Q_{out}(t)}\right) \propto \frac{N(t) l k_a}{V}, \tag{3.2}$$

where λ is the absorbance, Q_{in} is the light intensity entering the atom cloud, Q_{out} is the light intensity exiting the atom cloud, N is the relevant number of atoms inside

the volume of interest V as before, l is the length of the absorbing path and k_a is the absorbing coefficient. We remark that k_a is constant for a constant light frequency, as in our AAS setup.

Let us first determine a way to estimate the intensity of light entering the atom cloud Q_{in}. We would like this quantity to incorporate all the light loss resulting from the optic components. Accordingly, we take upon initialization

$$Q_{in}(0) = Q_{out}(0) = Q_s(0) - Q_b(0), \tag{3.3}$$

where Q_s is the measured light with the shutter opened, Q_b is the measured background light with the shutter closed. For the future quantification of this incident light intensity we can then use

$$Q_{in}(t) = \frac{Q_{in}(0)}{Q_{ref}(0)} Q_{ref}(t), \tag{3.4}$$

where Q_{ref} refers to the measured baseline intensity. For the propagation of $Q_{out}(t)$, we use

$$Q_{out}(t) = Q_s(t) - Q_b(t). \tag{3.5}$$

Combining (3.2), (3.4) and (3.5) accordingly yields

$$\lambda(t) = \log_{10}\left(\frac{Q_{in}(0)Q_{ref}(t)}{Q_{ref}(0)(Q_s(t) - Q_b(t))}\right). \tag{3.6}$$

The next step is to relate the absorbance of light to the sodium pressure, e.g. to perform the calibration. Let us consider a mapping $\Lambda = \Psi(\lambda)$, with Λ the measured sodium pressure in Pa. We obtain $\Psi(\lambda)$ by actively controlling the vapor pressure in our experimental setup through the temperature of the cooling element. It can be checked that the vapor pressure is primarily determined by the coldest surface, which essentially acts as an atom trap. The change in pressure is furthermore nearly instantaneous, because of the significantly smaller time scale of mass transport and sorption phenomena. For sodium, we can use the vapor pressure relation (Nesmeyanov 1963)

$$P_{Na} = \xi(T_c) = 133.322 \times 10^{7.4925 - \left(\frac{5370}{T_c}\right)}, \tag{3.7}$$

with P_{Na} the sodium pressure in Pascal and T_c the cold spot temperature in Kelvin. We can accordingly approximate the function $\Psi(\lambda)$ from the datasets. We will discuss the relation between $\xi(T_c)$ and $\Psi(\lambda)$ more extensively in Section 3.4.1.

3.3.2 Model implementation

Let us now proceed with obtaining the model components $f(\cdot)$ and $\dot{N}_s(\cdot)$ for our experiment. As shortly discussed in Section 3.2.3, we can derive a structure for the

function $f(\cdot)$ using (3.7). The intermediate steps can be found in Appendix 3.A. This procedure accordingly yields the structure

$$f(\bar{x}, T_r) = \left[b_1 \frac{\bar{x}}{T_r^2} + b_2 \frac{10^{\frac{b_3}{T_r}}}{T_r^{2.5}} \right] \dot{T}_r, \tag{3.8}$$

with b_1, b_2 and b_3 to be fitted.

We will evaluate the fluxes model in (2.5) for $n = 4$. We discretize the cylinder as follows; ω_1 is the cylinder bottom, ω_2 the lower half of the side, ω_3 the upper half of the side and ω_4 the top. The reference temperature $\dot{T}_r$ is accordingly associated with ω_4. Notice furthermore that (3.8) is zero for a constant surface temperature, such as we assume for the surfaces ω_1, ω_2 and ω_3. We then obtain

$$\begin{aligned}
\dot{x}(t) &= (A - \delta I)\bar{x}(t) - A \begin{bmatrix} 0 \\ 0 \\ 0 \\ 1 \end{bmatrix} \left[b_1 \frac{\bar{x}_4(t)}{T_r(t)^2} + b_2 \frac{10^{\frac{b_3}{T_r(t)}}}{T_r(t)^{2.5}} \right] \nu(t), \\
\dot{T}_r(t) &= \nu(t), \\
\bar{y}(t) &= \frac{2R}{V} \sqrt{\frac{T_r(t)\pi M}{8R}} \mathbb{1}^\top (p^A \cdot \ell) \bar{x}(t),
\end{aligned} \tag{3.9}$$

where $\bar{x}_4$ is the fourth entry of $\bar{x}$ and we consider only the top half of the cylinder volume for $h(\cdot)$, e.g. $0.5V$.

For the moles model, we derive $\dot{N}_s(\cdot)$ in a similar fashion as we did $f(\cdot)$. The steps can be found in Appendix 3.B. We accordingly have

$$\dot{N}_s(N, T_r) = \left[\frac{N}{T_r} + \frac{\beta_1 10^{\frac{\beta_2}{T_r}}}{T_r^3} \right] \dot{T}_r, \tag{3.10}$$

where $\beta_1 = -7.5909 \times 10^9$ and $\beta_2 = -5370$. We then have the full system as

$$\begin{aligned}
\dot{N}(t) &= \left[\frac{N(t)}{T_r(t)} + \frac{\beta_1 10^{\frac{\beta_2}{T_r(t)}}}{T_r(t)^3} \right] \nu(t), \\
\dot{T}_r(t) &= \nu(t), \\
\hat{y}(t) &= \frac{N(t) R T_r(t)}{V}.
\end{aligned} \tag{3.11}$$

We will now discuss the numerical values of constants used in the models. The deposition chamber is a glass cylinder with a height $\bar{H} = 0.102$m and a radius $\bar{R} = 0.062$m. It accordingly has a total volume $V = 1.23 \times 10^{-3}$ m^3. We furthermore have

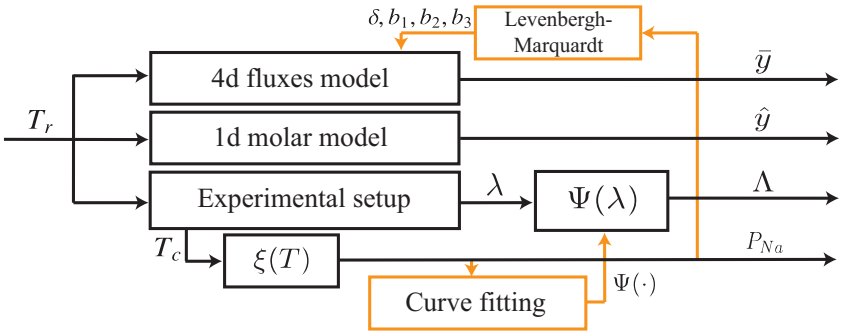

Figure 3.4: Origin of signal outputs for experimentation

We show the interaction of modeling components with our experimental setup. The experimental setup input $\dot{T}_r = \nu(t)$ is, together with its solution, also the input for the models. P_{Na} on the other hand, is determined from the measured cold spot temperature T_c. The orange parts in this diagram are the components used to fit the function Ψ and the parameters δ, b_1, b_2 and b_3, these parts are performed ex-situ. The black parts in the diagram belong to main system and can run real-time. The purpose of the experiment is to obtain and compare the outputs $\bar{y}$, $\hat{y}$, Λ and P_{Na}.

the gas constant $R = 8.3145 \frac{\text{J}}{\text{mol K}}$ and the moles mass of sodium $M = 0.0230 \frac{\text{kg}}{\text{mol}}$. For ℓ, the path length (in meters) of the directed fluxes through V, we will suffice with a crude approximation. We accordingly let

$$\ell = \begin{bmatrix} 0 & 0 & 0.025 & 0.05 \\ 0 & 0 & 0.05 & 0.075 \\ 0.025 & 0.05 & 0.1 & 0.1 \\ 0.05 & 0.075 & 0.1 & 0.1 \end{bmatrix}. \tag{3.12}$$

For the described geometry, we follow the procedures described in Section 2.3 to obtain the matrix p^A. In this case, since our discretization is similar to the discretization used in (Cale and Raupp 1990), we can derive it from transfer probability functions provided there. p^A is accordingly given by

$$p^A = \begin{bmatrix} 0 & 0.1373 & 0.3350 & 0.5277 \\ 0.1373 & 0.3300 & 0.1977 & 0.3350 \\ 0.3350 & 0.1977 & 0.3300 & 0.1373 \\ 0.5277 & 0.3350 & 0.1373 & 0 \end{bmatrix}. \tag{3.13}$$

We are then left with fitting the remaining parameters δ, b_1, b_2 and b_3. Such a fitting procedure is necessary, since the effect of A and δ on the sorptions is not directly clear (as discussed in Section 2.2.2). We apply the Levenberg-Marquardt algorithm with $e(t) = \bar{y}(t) - P_{Na}(t)$. For a smooth input signal $\nu(t)$, we can obtain the reference temperature profile of the cold spot $T_r(t)$ in accordance with (3.9). This

profile should be so that it covers the temperature domain of interest. The theoretical pressure inside the reactor can then be determined through (3.7), where we consider $P_{Na}(t) = \xi(T_r(t))$. The signal $\bar{y}(t)$ is then the associated model output for this temperature profile. Using this procedure, we obtain $\delta = 0.8112$, $b_1 = 3.3230$, $b_2 = -2.9914 \times 10^{12}$ and $b_3 = -5378.5$. Lastly, we have $A = \delta p^A$.

The relation between all obtained variables and functions is shown in Fig. 3.4. In this figure, the orange parts relate to the system identification parts of the modeling. The black parts will be used to assess performance during the experimentation.

3.4 Experimental results and discussion

We are now ready to present our experimental results. To this end, we will first discuss our AAS sensor performance and calibration and how we obtain $\Psi(\cdot)$, followed by a comparison of the four sodium pressure signals depicted in Fig 3.4. We evaluate the performance of the components by applying a sinusoidal reference temperature signal T_r to our cold spot. For this signal and its derivative we use

$$T_r(t) = 30 \cos\left(\frac{\pi t}{5400}\right) + 403.15, \tag{3.14}$$

$$\dot{T}_r(t) = -\frac{\pi}{180} \sin\left(\frac{\pi t}{5400}\right). \tag{3.15}$$

The applied and realized temperature profiles are shown in Fig. 3.5.

3.4.1 AAS sensor assessment and calibration

We assess the performance of our sensor by evaluating deviation in the measured absorbance between the three cycles shown in Fig. 3.5. The results are shown in Fig. 3.6. The deviation between the cycles is very small, indicating that the measurements are reproducible with small relative error. It is furthermore apparent that the graph displays the symmetry from the cold spot temperature reference (3.14). This confirms that we are operating strictly in the vapor pressure regime and that the pressures shown in Fig. 3.6 are good estimations of sodium pressure in the reactor.

The relation between the absorbance λ, the sodium pressure P_{Na} and the cold spot temperature T_c is shown more explicitly in Fig. 3.7. Based on the Beer-Lambert law (3.2) and the ideal gas law (2.2), we would expect the relation between λ and P_{Na} to satisfy

$$P_{Na} \propto \frac{\lambda l k_a R T_a}{V^2}, \tag{3.16}$$

where l, R and V are constants and k, the absorbing coefficient, is constant for constant light frequencies, which holds for this experiment. The temperature of the atom cloud T_a is the only factor that could cause the non-proportionality of the function

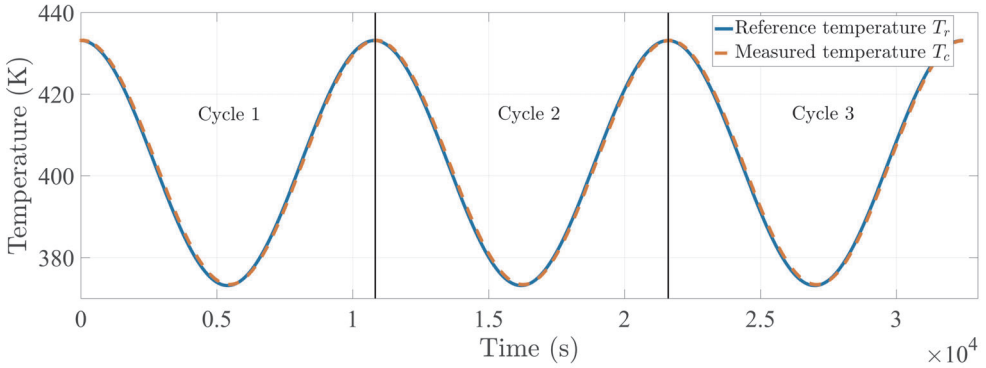

Figure 3.5: Applied and realized temperature signals for experiments.

The reference and realized cold spot temperature profiles are shown. The reference profile is generated in accordance with (3.14) *and* (3.15)*. We can identify three cosine cycles applied during the experiment, which we will compare to investigate measurement reproducibility. The graph furthermore shows that the applied proportional control loop is able to track the reference with a small delay. The length of the cosine cycle is determined by physical constraints, where in particular the heating of the cold spot is rate restricted since we only control the flow of a cooling air stream to this part of the reactor.*

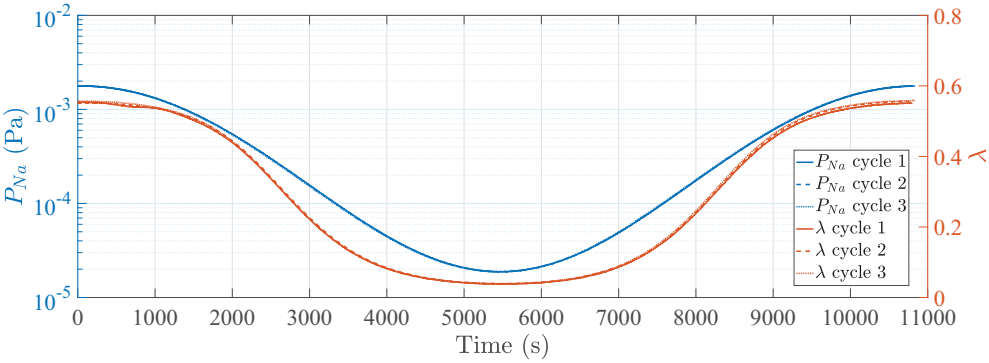

Figure 3.6: Comparison of measured absorbances and associated pressures

This figure depicts the measured absorbance λ and derived vapor pressure $P_{Na} = \xi(T_c)$ evolution over time for the three cosine temperature cycles depicted in Fig 3.5. The measurement results feature excellent reproducibility, which is apparent because the subsequent cycles are very close to each other.

shown in Fig. 3.7, according to (3.16). However, dividing the pressure by the cold spot temperature T_c, which should then possibly cause an over-correction due the relatively strong temperature changes, does not yield a proportional slope. These results accordingly show that there is a discrepancy between the combined Beer-Lambert law (3.2) and ideal gas law (2.2) on the one side, and the sodium vapor pressure equation (3.7) on the other side. It is likely that the semi-empirical func-

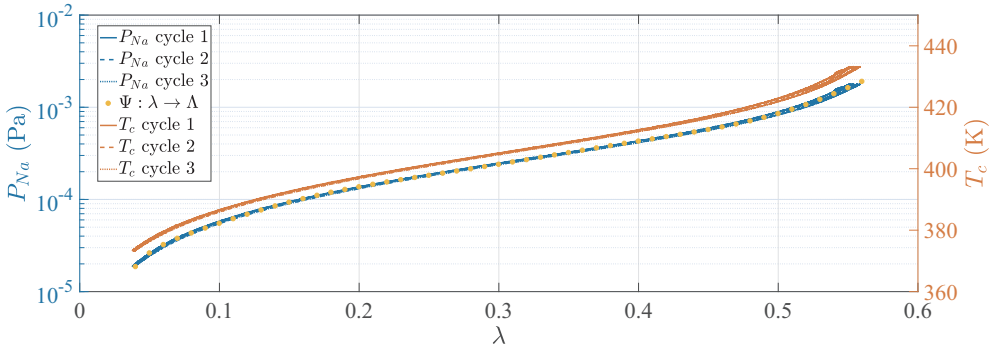

Figure 3.7: Relation between measured absorbances, temperatures and pressures

We show the relations between the measured absorbance λ, the pressure P_{Na} and the temperature of the cold spot T_c. We furthermore show the function $\Psi : \lambda \to \Lambda$, for $\lambda \in [0.0375, 0.56]$, as in (3.17)*. The relation between the absorbance and the temperature depicted here only holds in the vapor pressure regime. The relation between the absorbance and the pressure holds outside this regime as well.*

tion (3.7) is the main cause of this, as there are multiple candidate forms for such functions and problems with experimental apparatus compromising the accuracy of obtained results are frequently reported in (Nesmeyanov 1963). Perhaps the methods developed and applied in this chapter can be used to improve understanding on this issue in the future.

As discussed above and shown in Fig. 3.7, the mapping $\Psi : \lambda \to \Lambda$ cannot be described by a simple proportional relation. We will therefore use a polynomial mapping instead. Such a mapping can easily be fitted to the data. We will use

$$\Psi(\lambda) = 7.138\lambda^7 - 12.29\lambda^6 + 8.498\lambda^5 - 3.005\lambda^4 + 0.5775\lambda^3 - 0.05822\lambda^2 + 0.003415\lambda - 5.495 \times 10^{-5}, \quad (3.17)$$

which holds for $\lambda \in [0.0375, 0.56]$. Function (3.17) is shown graphically in Fig. 3.7.

3.4.2 Comparison of theoretical vapor pressure, model and sensor performance

We are now ready to compare the sodium pressure signals P_{Na}, Λ, $\bar{y}$ and y. We initialize the simulations so that $y(0) \approx \bar{y}(0) \approx P_{Na}(0) = \xi(433.15)$. The four signals are shown in Fig. 3.8. We furthermore show three errors that take P_{Na} as a benchmark; $e_\Lambda = \frac{|\Lambda - P_{Na}|}{P_{Na}}$, $e_{\bar{y}} = \frac{|\bar{y} - P_{Na}|}{P_{Na}}$ and $e_{\hat{y}} = \frac{|\hat{y} - P_{Na}|}{P_{Na}}$.

Fig. 3.8 shows that all errors are significantly smaller in magnitude than the pressure P_{Na} that is being evaluated. We furthermore see that the accuracy of the measurement Λ is in the same range as the accuracy for the 1d moles model output $\bar{y}$ and the 4d fluxes model output y. The results accordingly show that all three obtained

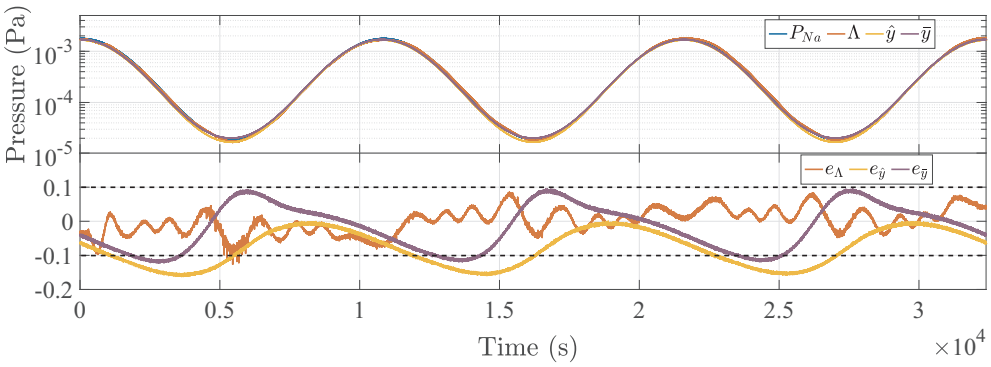

Figure 3.8: Comparison of model outputs, measured and theoretical pressures

A comparison between the theoretical vapor pressure P_{Na}, the measured vapor pressure Λ, the estimated vapor pressure from the moles model $\bar{y}$ and the estimated vapor pressure from the fluxes model y is shown. The normalized absolute errors $e_\Lambda = \frac{|\Lambda - P_{Na}|}{P_{Na}}$, $e_{\bar{y}} = \frac{|\bar{y} - P_{Na}|}{P_{Na}}$ and $e_{\hat{y}} = \frac{|\hat{y} - P_{Na}|}{P_{Na}}$ are shown in the same graph and with the same color and their corresponding signals to highlight the differences in magnitude.

signals are suitable for estimations of the sodium pressure P_{Na}. We can thus use the measurement Λ in combination with either the moles model or the fluxes model as a starting point for UHVCVD partial pressure controller design.

3.5 Concluding remarks

We have used this chapter to introduce the AAS-based partial pressure measurement and an experimental setup design that implements this measurement. This setup is subsequently used to validate both the AAS-based measurement and the flux-based dynamical model from Chapter 2.

We found that the AAS-based partial pressure measurements yields reproducible results with very high resolution. Careful calibration of such a sensor is essential, as it will correct for any changes in the optical configuration. The dual beam configuration with shutter that we have applied furthermore allows for a minimization of other disturbing factors, to a level where they were practically non-existent for our application.

The flux-based model from Chapter 2 has proven to be capable of predicting partial pressures while operating in vapor pressure conditions. This result complements the results presented in Chapter 2. We have now shown that the model is not only theoretically suitable for model-based controller design for some chemical processes that have FMF dynamics, but can furthermore be used to describe the vapor pressure dynamics in practice.

With the results from this chapter, we are ready for more rigorous identification of the flux-based model for UHVCVD applications. The identified model can sub-

sequently be used for the model-based controller design. However, identification of the model is bound to be a challenging project in its own right. In this chapter, we have conveniently used available vapor pressure functions from the literature to derive part of the dynamics. However, in a general case, such a function is not directly available. We excluded another part of the dynamics by not modeling the precursor evaporation process. The evaporation process is however an essential factor during depositions and should therefore be incorporated in the model. What further exacerbates the identification challenge is that we are dealing with a system where little (real-time) information on the states is available.

The next step in realizing partial pressure control for the UHVCVD process is to realize a controller design. Such a controller design is preferably model-based, but we estimate the model identification of the flux-based model to be costly and time consuming. We will therefore first focus our attention on controller designs that do not require such an extensive identification process. This is presented in the next chapter.

3.A Sorption for the fluxes model

We require f to be so that the fluxes $\bar{x}$ satisfy

$$P_{Na} = h(\bar{x}, T_a), \tag{3.18}$$

for all t, with T_a the average temperature of the atom cloud and P_{Na} in Pascal. Indeed, for our experiment with only sodium present inside the reactor, no leakage and no evaporation, $f(\cdot)$ acts as a function that includes the vapor pressure phenomena in the dynamics. The vapor pressure can be related to temperature by empirical functions. Let us accordingly consider the function $\xi(T_c)$ from (3.7). We then have the requirement

$$\xi(T_c) = h(\bar{x}, T_a), \tag{3.19}$$

or equivalently;

$$\frac{\partial \xi(T_c)}{\partial T_c}\dot{T}_c = \frac{\partial h(\bar{x}, T_a)}{\partial \bar{x}}\dot{\bar{x}} + \frac{\partial h(\bar{x}, T_a)}{\partial T_a}\dot{T}_a. \tag{3.20}$$

Rewriting yields

$$\frac{\partial h(\bar{x}, T_a)}{\partial \bar{x}}\dot{\bar{x}} = \frac{\partial \xi(T_c)}{\partial T_c}\dot{T}_c - \frac{\partial h(\bar{x}, T_a)}{\partial T_a}\dot{T}_a. \tag{3.21}$$

We consider a simplified case with $n = 1$, $g(u(t), t) = 0$ and $L = 0$. By substitution of $\dot{\bar{x}}$ with (2.5), we obtain

$$-\frac{\partial h(\bar{x}, T_a)}{\partial \bar{x}}\delta f(\bar{x}, T) = \frac{\partial \xi(T_c)}{\partial T_c}\dot{T}_c - \frac{\partial h(\bar{x}, T_a)}{\partial T_a}\dot{T}_a. \tag{3.22}$$

Let us then denote

$$\zeta = \frac{R}{V}\sqrt{\frac{\pi M}{8R}}\ell. \tag{3.23}$$

We obtain for the partial derivatives

$$\frac{\partial h(\bar{x}, T_a)}{\partial \bar{x}} = \zeta\sqrt{T_a}, \tag{3.24}$$

$$\frac{\partial h(\bar{x}, T_a)}{\partial T_a} = \frac{\zeta}{2\sqrt{T_a}}\bar{x}(t), \tag{3.25}$$

$$\frac{\partial \xi(T_c)}{\partial T_c} = \frac{a_1 10^{\frac{a_2}{T_c}}}{T_c^2}, \tag{3.26}$$

with $a_1 = 5.1238 \times 10^{13}$ and $a_2 = -5370$. Care needs to be taken with the function ξ. Indeed, this function is essentially a mapping from the coldest surface to the sodium pressure, meaning it will not hold for all surfaces regardless. Let us place an assumption of uniformity for the interpretation of ξ. This means, that we let all temperature T_c, T_a and T be equal to T. The interpretation is that the atoms in the cloud take the temperature of the surfaces, which are uniform. We accordingly obtain

$$-\frac{\partial h(\bar{x}, T)}{\partial \bar{x}}\delta f(\bar{x}, s, T) = \left[\frac{\partial \xi(T)}{\partial T} - \frac{\partial h(\bar{x}, T)}{\partial T}\right]\dot{T}, \tag{3.27}$$

$$f(\bar{x},T)=\left[-\frac{\partial h(\bar{x},T)}{\partial \bar{x}}\delta\right]^{-1}\left[\frac{\partial \xi(T)}{\partial T}-\frac{\partial h(\bar{x},T)}{\partial T}\right]\dot{T}. \tag{3.28}$$

Which, through substitutions of the partial derivatives, yields

$$f(\bar{x},T)=\left[-\frac{a_1 10^{\frac{a_2}{T}}}{\delta\zeta T^{2.5}}+\frac{\bar{x}}{2\delta T}\right]\dot{T} \tag{3.29}$$

or equivalently

$$f(\bar{x},T)=\left[b_1\frac{\bar{x}}{T}+b_2\frac{10^{\frac{b_3}{T}}}{T^{2.5}}\right]\dot{T}, \tag{3.30}$$

where b_1, b_2 and b_3 are to be fitted.

3.B Sorption for the moles model

This procedure is similar to the one used in 3.A. We start out with

$$\xi(T)=\frac{NRT}{V}, \tag{3.31}$$

which is based on the ideal gas law. Differentiating yields

$$\frac{\partial \xi(T)}{\partial T}\dot{T}=\frac{\dot{N}RT}{V}+\frac{NR\dot{T}}{V} \tag{3.32}$$

$$\frac{a_1 10^{\frac{a_2}{T}}}{T^2}\dot{T}=-\frac{\dot{N}_s RT}{V}+\frac{NR\dot{T}}{V}, \tag{3.33}$$

with $a_1=5.1238\times 10^{13}$ and $a_2=-5370$. Solving for $\dot{N}_s$ then yields

$$\dot{N}_s=\left[\frac{N}{T}+\frac{\beta_1 10^{\frac{\beta_2}{T}}}{T^3}\right]\dot{T}, \tag{3.34}$$

with $\beta_1=-7.5909\times 10^9$ and $\beta_2=-5370$.